Optimal Disturbances in the Supersonic Boundary Layer Past a Sharp Cone

Simone Zuccher*, Ivan Shalaev† and Anatoli Tumin‡
University of Arizona, Tucson, AZ, 85721, USA

Eli Reshotko§
Case Western Reserve University, Cleveland, OH, 44106, USA

Optimal disturbances for the supersonic flow past a sharp cone are computed in order to assess the effects due to flow divergence. This geometry is chosen because previously published studies on compressible optimal perturbations for flat plate and sphere did not allow to discriminate the influence of divergence alone, as many factors characterized the growth of disturbances on the sphere (flow divergence, centrifugal forces and dependence of the edge parameters on the local Mach number). Flow-divergence effects result in the presence of an optimal distance from the cone tip for which the optimal gain is the largest possible, showing that divergence effects are stronger in the proximity of the cone tip. By properly rescaling the gain, wavenumber and streamwise coordinate due to the fact that the boundary layer on the sharp cone is $\sqrt{3}$ thinner than the one over the flat plate, it is found that both the gain and the wavenumber compare fairly well. Moreover, results for the sharp cone collapse into those for the flat plate when the initial location for the computation tends to the final one and when the azimuthal wavenumber is very large. Results show also that a cold wall enhances transient growth.

I. Introduction

In many applications transition to turbulence occurs without the classical exponential growth. On the contrary, a transient growth of the disturbance energy and a subsequent downstream decay is observed in flows that are stable to wave-like perturbations such as Tollmien–Schlichting (TS) waves. The problem of optimal disturbances, in the context of bypass transition to turbulence, has been of great interest during the last decade.

Transient growth arises from the coupling between slightly damped, highly oblique Orr-Sommerfeld (OS) and Squire modes leading to algebraic growth followed by exponential decay, in subcritical regions outside the TS neutral curve. A weak transient growth can also occur for two-dimensional modes since the OS operator and its compressible counterpart are not self-adjoint, and therefore their eigenfunctions are not strictly orthogonal.[1]

Historically, the first approach to nonmodal disturbances was in the inviscid limit and in the temporal framework, where it was found that the streamwise disturbance velocity amplitude may grow algebraically in time, even though the basic flow does not posses an inflection point.[2] Several other pioneering works followed[3,4,5,6,7,8,9] in the temporal framework, recognizing the great potential of nonmodal growth for explaining bypass transition. For a brief account on the development of transient-growth studies, not only in classical fluid mechanics but also in meteorology, the reader is referred to Ref. 10

Optimal perturbations in the spatial framework have only more recently been considered. The spatial Cauchy problem within the scope of the linearized Navier–Stokes equations is, however, radically different from the temporal one and ill posed,[10,11] raising some obstacles in applying to the spatial analysis the same

*Research Assistant Professor, Department of Aerospace and Mechanical Engineering, AIAA Member.
†Graduate Student, Department of Aerospace and Mechanical Engineering.
‡Associate Professor, Department of Aerospace and Mechanical Engineering, AIAA Associate Fellow.
§Kent H. Smith Professor Emeritus of Engineering, Department of Mechanical and Aerospace Engineering, AIAA Fellow.

optimization methods used in the temporal case. The ill-posedness of the spatial Cauchy problem was first overcome by considering the (linearized) boundary layer equations[12,13] instead of the Navier–Stokes equations, and including nonparallel effects. The optimal initial disturbance was found to be composed of stationary streamwise vortices whereas the induced velocity field was dominated by streamwise streaks. In the spatial framework, optimal perturbations have also been computed in the nonlinear case.[14]

In the compressible case, and within the scope of the parallel flow approximation, temporal[15,16] and spatial[17,18,19] analyses of the transient growth phenomenon have been carried out. A model for transient growth including non-parallel effects in the compressible boundary layer past a flat plate has also been developed[20] and then extended to the compressible boundary layer past a sphere.[19,10,11] In Refs. 10, 11 compressible optimal perturbations were calculated by including surface curvature effects and non-parallel growth of the boundary layer. Moreover, the use of a full energy norm at the inlet[10] and at the outlet[10,11] was considered, motivated by fact that in a flow field dominated by streamwise vortices, the wall-normal and spanwise velocity components at the outlet might also play a role in the energy norm to be maximized. This could be the case of a blunt body, for which there are some indications that the largest transient growth is located close to the stagnation point,[21] where a flow field dominated by streaks might not yet been established.

Despite the efforts done insofar, some issues regarding transition in supersonic flows are still open. One of them is the long-standing blunt-body paradox,[17] according to which transition occurs in supersonic flows behind the detached bow shock, in a region that is subsonic and characterized by a favorable pressure gradient and therefore stable to TS-instability-like phenomena. Transient growth seems to be a promising mechanism to explain such a paradox.[10] However, the ultimate elucidation of the blunt-body paradox requires solving the roughness receptivity problem, which can explain the origin of the perturbation. The latter issue has not been addressed yet.

In the previously cited works concerning the compressible boundary layer past a sphere,[10,11] several effects contribute to the results, such as the geometrical divergence of the flow (in the azimuthal direction), the centrifugal forces (in the streamwise direction), and the indirect dependence of the edge conditions (at the edge of the boundary layer) on the Mach number through the meridional coordinate. On the contrary, the supersonic boundary layer past a flat plate does not include any of these effects. A comparison between flat-plate results and sharp-cone results, on the other hand, would shed some light on the role played by flow divergence, due to geometrical factors only. In the case of sharp cone, in fact, there are no centrifugal forces and the Mach number is constant in the streamwise direction, excluding two out of three effects present in the compressible boundary layer past a sphere. An analysis of the optimal perturbations in the supersonic flow over a sharp cone is, however, still missing.

The objective of the present work is therefore the characterization of optimal disturbances in the supersonic boundary layer over a sharp cone. The aim is twofold. Results here obtained, when compared with the flat-plate and sphere cases, will elucidate the role played by the flow divergence alone. Secondly, the extension to the axisymmetric case of the sharp cone represents an intermediate step towards the computation of optimal perturbations in the supersonic boundary layers for more realistic geometries, such as the blunt-nose cone and three-dimensional geometries.

II. Governing equations

The governing equations for steady, three-dimensional disturbances in the supersonic flow past a sharp cone are derived from the linearized Navier–Stokes equations, in the same fashion as in Refs. 20, 19, 10, 11.

A small parameter $\epsilon = H_{\mathrm{ref}}/L_{\mathrm{ref}}$ is introduced for scaling purposes, where $H_{\mathrm{ref}} = \sqrt{\nu_{\mathrm{ref}} L_{\mathrm{ref}}/U_{\mathrm{ref}}}$ is a typical-boundary layer length in the wall-normal direction y and L_{ref} is a typical scale of the geometry (length of cone L in the present case). The scaling parameter ϵ is thus strictly related to the Reynolds number $\epsilon = Re_{\mathrm{ref}}^{-1/2}$, where $Re_{\mathrm{ref}} = U_{\mathrm{ref}} L_{\mathrm{ref}}/\nu_{\mathrm{ref}}$ is the reference Reynolds number.

As it follows from previous works regarding optimal perturbations in both incompressible and compressible boundary layers,[13,22,19,23,14,10,11] the disturbance flow is expected to be dominated by streamwise vortices and therefore the following scaling is employed.[10] The streamwise coordinate x is normalized with L_{ref}, whereas the wall-normal coordinate y is scaled with $\epsilon L_{\mathrm{ref}}$. The azimuthal coordinate ϕ, being an angle, is not normalized. The streamwise velocity component u is scaled with U_{ref}, wall-normal velocity v and azimuthal velocity w with $\epsilon U_{\mathrm{ref}}$, temperature T with T_{ref} and pressure p with $\epsilon^2 \rho_{\mathrm{ref}} U_{\mathrm{ref}}^2$. Density ρ is eliminated through the state equation.

Due to the scaling adopted, the second derivative with respect to the streamwise coordinate x is smaller than the other terms, and is therefore neglected. This leads to a change in the nature of the equations from elliptic (Navier–Stokes equations) to parabolic.

Perturbations are assumed to be periodic in the azimuthal direction ϕ as $\exp(im\phi)$, where m is the azimuthal index, so that the general unknown can be expressed as $q(x,y)\exp(im\phi)$, where $q(x,y)$ is the amplitude, which depends on x and y, and i is the imaginary unit.

If the vector of perturbations is $\mathbf{f} = [u, v, w, T, p]^{\mathrm{T}}$ (where the superscript $^{\mathrm{T}}$ denotes the transpose), with $w = \mathrm{i}\tilde{w}$ ($\tilde{w}$ being the amplitude of the spanwise velocity component), the governing equations can be written as follows:

$$(\boldsymbol{A}\mathbf{f})_x = (\boldsymbol{D}\mathbf{f}_y)_x + \boldsymbol{B}_0\mathbf{f} + \boldsymbol{B}_1\mathbf{f}_y + \boldsymbol{B}_2\mathbf{f}_{yy}. \tag{1}$$

This form of the governing equations is general and can be derived for different geometries such as flat plate, sphere, sharp cone or blunt-nose cone. Nonzero elements of the 5 by 5 real matrices $\boldsymbol{A}$, $\boldsymbol{B}_0$, $\boldsymbol{B}_1$, $\boldsymbol{B}_2$ and $\boldsymbol{D}$ are reported in appendix A. New terms, relative to the flat-plate case, arise in the equation due to the geometrical factor introduced by the half-angle of the cone tip θ.

As far as boundary conditions are concerned, all perturbations are required to be zero at the wall except for p, while in the freestream all perturbations vanish except for v:

$$\begin{aligned} y = 0: &\quad u = 0; v = 0; w = 0; T = 0 \\ y \to \infty: &\quad u \to 0; w \to 0; p \to 0; T \to 0 \end{aligned} \tag{2}$$

In order to isolate the derivative with respect to x, system (1) can be recast as

$$(\boldsymbol{H}_1\mathbf{f})_x + \boldsymbol{H}_2\mathbf{f} = 0, \tag{3}$$

where operators $\boldsymbol{H}_1$ and $\boldsymbol{H}_2$ are still 5 by 5 real matrices and contain the dependence on x and y due to the basic flow:

$$\boldsymbol{H}_1 = \boldsymbol{A} - \boldsymbol{D}(\cdot)_y; \qquad \boldsymbol{H}_2 = -\boldsymbol{B}_0 - \boldsymbol{B}_1(\cdot)_y - \boldsymbol{B}_2(\cdot)_{yy}. \tag{4}$$

System (3) is parabolic in nature and can be solved by means of a downstream marching procedure with initial data specified at the inlet section of the domain $x = x_{\mathrm{in}}$.

It is worth noting that the disturbance equations are not Reynolds-number independent (contrary to the flat-plate case) because of the parameter ϵ in the scaling, which is associated with geometrical effects.

III. Formulation of the optimization problem

The problem of finding arbitrarily normalized optimal perturbations practically reduces to performing a constrained optimization. The constraints are the governing equations (3) and the normalization of the initial condition, i.e. $E_{\mathrm{in}} = E_0$, E_{in} being the energy of the perturbation at the inlet and E_0 a constant (typically 1). The objective function is a particular norm to be identified, and therefore arbitrary. However, it should be a measure of the flow conditions relevant to the transition process. This choice is neither easy nor unique. In previous works dealing with optimal perturbations in the incompressible framework,[12,13,22,23,14] the kinetic energy of the disturbance field has always been the choice.

In the compressible case, previous works[20,19,10,11] maximized Mack's energy norm[24] of the perturbation kinetic energy, density, and temperature (or simply the part containing u and T) in the outlet plane,

$$E_{\mathrm{out}} = \int_0^\infty \left[\rho_{s\,\mathrm{out}}\left[u_{\mathrm{out}}^2 + \epsilon^2(v_{\mathrm{out}}^2 + w_{\mathrm{out}}^2)\right] + \frac{\rho_{\mathrm{out}}^2 T_{s\,\mathrm{out}}}{\gamma\rho_{s\,\mathrm{out}}M^2} + \frac{T_{\mathrm{out}}^2\rho_{s\,\mathrm{out}}}{\gamma(\gamma-1)T_{s\,\mathrm{out}}M^2}\right] dy, \tag{5}$$

in which the scaling described in §II is employed. Expression (5) was derived for perturbations developing in the boundary layer over a flat plate within the temporal framework, and is here utilized for the spatial one, as done in Ref. 20. After employing the equation of state for the basic flow and for the perturbation, and observing that in the limit $\epsilon \to 0$ v and w can be neglected (Reynolds-independent approach, see Ref. 13), the norm reads

$$E_{\mathrm{out}} = \int_0^\infty \left[\rho_{s\,\mathrm{out}}u_{\mathrm{out}}^2 + \frac{p_{s\,\mathrm{out}}T_{\mathrm{out}}^2}{(\gamma-1)T_{s\,\mathrm{out}}^2M^2}\right] dy, \tag{6}$$

or more compactly

$$E_{\mathrm{out}} = \int_0^\infty \left(\mathbf{f}_{\mathrm{out}}^T\widetilde{\boldsymbol{M}}_{\mathrm{out}}\mathbf{f}_{\mathrm{out}}\right) dy, \tag{7}$$

where the linear operator $\widetilde{\boldsymbol{M}}_{\text{out}}$ is the diagonal 5×5 matrix

$$\widetilde{\boldsymbol{M}}_{\text{out}} = \begin{bmatrix} \rho_{s\,\text{out}} & 0 & 0 & 0 & 0 \\ 0 & 0 & 0 & 0 & 0 \\ 0 & 0 & 0 & 0 & 0 \\ 0 & 0 & 0 & \dfrac{p_{s\,\text{out}}}{(\gamma-1)T_{s\,\text{out}}^2 M^2} & 0 \\ 0 & 0 & 0 & 0 & 0 \end{bmatrix}. \tag{8}$$

The initial condition for the compressible boundary-layer equations is not arbitrary, but only three of the five variables can be imposed at x_{in}.[25] However, in the incompressible case and for $Re \to \infty$, it was observed that the choice $u_{\text{in}} = 0$, $p_{\text{in}} = 0$, v_{in} and w_{in} related by the continuity equation guarantees the maximum gain in an input-output fashion[13] (in the incompressible case the number of independent initial conditions is two; see also Refs. 26, 13, 27). This choice also corresponds to the physical mechanism, observed in transitional boundary-layer flows, known as the lift-up effect,[28] according to which streamwise vortices lift low momentum flow up (from the wall) and push down high momentum flow causing streaks that eventually break down to turbulence. Led by these considerations, here we focus on initial perturbations with only v and w nonzero, which correspond to steady, streamwise vortices.

The kinetic energy of the optimal disturbance $\mathbf{f}_{\text{in}}$, if only v_{in} and w_{in} are nonzero, is therefore:

$$E_{\text{in}} = \int_0^\infty \left[\rho_{s\,\text{in}} \epsilon^2 (v_{\text{in}}^2 + w_{\text{in}}^2)\right] dy, \tag{9}$$

or more compactly

$$E_{\text{in}} = \int_0^\infty \left(\mathbf{f}_{\text{in}}^T \widetilde{\boldsymbol{M}}_{\text{in}} \mathbf{f}_{\text{in}}\right) dy, \tag{10}$$

where $\widetilde{\boldsymbol{M}}_{\text{in}}$ is the 5×5 diagonal matrix

$$\widetilde{\boldsymbol{M}}_{\text{in}} = \begin{bmatrix} 0 & 0 & 0 & 0 & 0 \\ 0 & \epsilon^2 \rho_{s\,\text{in}} & 0 & 0 & 0 \\ 0 & 0 & \epsilon^2 \rho_{s\,\text{in}} & 0 & 0 \\ 0 & 0 & 0 & 0 & 0 \\ 0 & 0 & 0 & 0 & 0 \end{bmatrix}. \tag{11}$$

The quantity to be maximized is $G = E_{\text{out}}/E_{\text{in}}$, the ratio between the outlet and inlet norms. However, in order to allow direct comparison with previous works, $G\epsilon^2$ will be presented in the results section

$$G\epsilon^2 = \frac{\displaystyle\int_0^\infty \left[\rho_{s\,\text{out}} u_{\text{out}}^2 + \frac{p_{s\,\text{out}} T_{\text{out}}^2}{(\gamma-1)T_{s\,\text{out}}^2 M^2}\right] dy}{\displaystyle\int_0^\infty \left[\rho_{s\,\text{in}} (v_{\text{in}}^2 + w_{\text{in}}^2)\right] dy}. \tag{12}$$

Since the problem is linear, an arbitrary normalization for the initial disturbance at x_{in} can be chosen, e.g. $E_{\text{in}} = E_0 = 1$, so that the maximization of (12) turns out to be equivalent to the maximization of expression (7), i.e. $\mathcal{J} = E_{\text{out}}$.

It should be clear now that the whole problem of finding optimal perturbations reduces to a constrained optimization, in which we seek the initial conditions for the disturbance equations (3) that maximize (7) and that satisfy the constraint $E_{\text{in}} = E_0$ at x_{in}, together with the direct equations (3) and boundary conditions (2) at each $x \in (x_{\text{in}}; x_{\text{out}})$.

The details of the constrained optimization procedure are not reported here, as they can be found in Refs. 10, 11, to which the Reader is referred. The classical Lagrange multiplier technique is applied to the discrete version of problem (3), which can be recast as $\boldsymbol{C}_{n+1}\mathbf{f}_{n+1} = \boldsymbol{B}_n \mathbf{f}_n$, leading to the so-called adjoint equations[26, 29, 13, 22, 23, 14, 10, 11] (here n denotes the n-th grid node in the streamwise direction x, $\mathbf{f}$ is the vector of $5 \times N_y$ unknowns at each n station, N_y being the number of grid nodes in the wall-normal direction y; matrices $\boldsymbol{C}$ and $\boldsymbol{B}$ depend on x and y, as the basic flow does, and account for the discretization in both x and y).

The use of the discrete approach has several advantages among which the necessity of an "ad hoc" adjoint code is avoided and a foolproof test is available by comparing the results of the direct and adjoint calculation, which must match up to machine accuracy for any step size and not only in the limit of step size tending to zero.[26,13,14]

The augmented functional $\mathcal{L}$, which contains the objective function $\mathcal{J} = E_{\text{out}}$, the constraints (3) and $E_{\text{in}} = E_0$, and the Lagrange multipliers, is then manipulated by adding and subtracting a certain quantity so as to rewrite it in a way more suited for its differentiation.[10,11] The optimization imposes $\delta\mathcal{L} = 0$, which leads to the adjoint equations in the discrete form and coupling conditions between the direct and adjoint problems at the inlet (x_{in}) and outlet (x_{out}). These conditions can be written in a matrix form so that their application becomes straightforward. In order to retrieve the outlet conditions, a system needs to be solved where the coefficient matrix is singular (due to $p_x = 0$ in this approximation), reflecting the fact that at least one out of five adjoint variables is free at $x = x_{\text{out}}$ and therefore can be chosen arbitrarily. For sake of simplicity, we set p_5 (the fifth adjoint variable) to zero.

The constrained optimization formulation requires the simultaneous solution of a large, coupled system of direct equations, adjoint equations, boundary conditions and coupling conditions. Instead of doing it in one shot, however, we employ the intrinsic parabolic nature of the equations to efficiently solve separately the two coupled problems. Such an algorithm can be outlined in the following few steps. (1) a guessed initial condition $\mathbf{f}_{\text{in}}^{(0)}$ is provided at the beginning of the optimization procedure; (2) the forward problem is solved at the i-th iteration with the initial condition $\mathbf{f}_{\text{in}}^{(i)}$; (3) the objective function $\mathcal{J}^{(i)} = E_{\text{out}}^{(i)}$ is computed at the end of the forward iteration and compared to the objective function $\mathcal{J}^{(i-1)} = E_{\text{out}}^{(i-1)}$ at the end of the previous forward iteration. If $|\mathcal{J}^{(i)}/\mathcal{J}^{(i-1)} - 1| < \epsilon_t$ (where ϵ_t is the maximum tolerance accepted to stop the optimization) then the optimization is considered converged and the problem solved; (4) if $|\mathcal{J}^{(i)}/\mathcal{J}^{(i-1)} - 1| > \epsilon_t$ the initial conditions for the backward problem are assigned at the outlet and derived from the direct solution at $x = x_{\text{out}}$; (5) the backward problem is solved from $x = x_{\text{out}}$ to $x = x_{\text{in}}$; (6) a new initial condition for the forward problem $\mathbf{f}_{\text{in}}^{(i+1)}$ is obtained from the solution of the backward problem at $x = x_{\text{in}}$ employing the coupling condition at the inlet; (7) the loop is repeated from step (2) on until it is eventually ended in step (3). It should be noted that this procedure does not necessarily guarantee convergence. If there is an attractor for the solution, then the procedure will capture it and this happens quite fast (2-3 forward-backward iterations).

IV. Discretization

A finite difference discretization scheme has been implemented to numerically solve equations (3) with boundary conditions (2). For the sake of generality, grid nodes in x and y are not necessarily equally spaced. A staggered grid is introduced in the wall-normal direction, with variables u, v, w and T known at the grid nodes, and p known at the mid-grid (staggered) nodes. All equations are satisfied at the grid nodes except for continuity, which is satisfied in the mid-grid nodes. The use of the uneven grid in y allows us to cluster more nodes close to the wall so as to take into account the larger gradients of boundary layer quantities in this region. The last node of the y-grid is located far enough from the wall to allow us to specify there the boundary conditions for $y \to \infty$.

Fourth-order non-compact finite differences are used for the y discretization, employing six nodes so as to allow 4th order accuracy for the second derivative. By using six nodes, the first derivative is automatically 5th order accurate and the function (when interpolated due to the staggered grid) is 6th order accurate.

Also the discretization in the streamwise direction is based on an uneven grid. Since the system of boundary layer equations is parabolic, a second order backward discretization is chosen, which requires the solution at two previous steps to be known. For the first step, however, a first order scheme is used because only the initial condition is available.

For further details and for the thorough derivation of the discrete adjoint equations, the Reader is referred to Refs. 10, 11.

V. Results

The basic flow for the sharp cone is obtained from the flat-plate case by rescaling the wall-normal coordinate y and its derivatives according to Mangler's transformations.[30] The local Mach number, M_{loc},

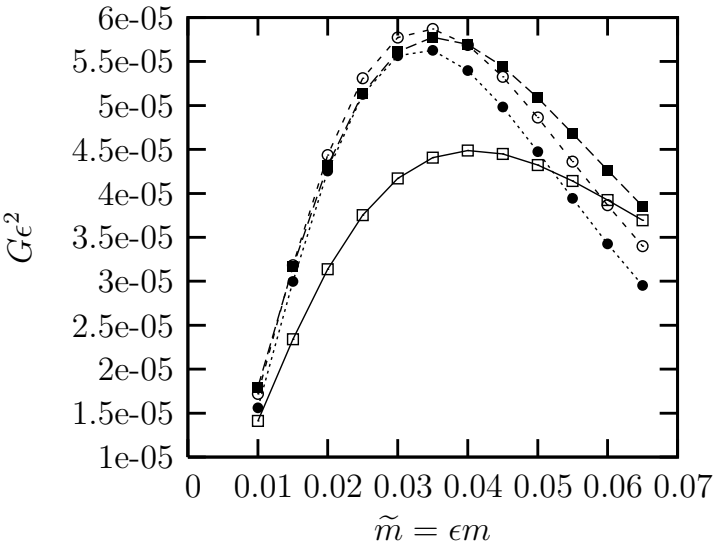

Figure 1. Objective function $G\epsilon^2$: effect of x_{out} and $\widetilde{m}$ for $\theta = 15°$, $M_\infty = 6$, $M_{\text{loc}} = 4.367$, $T_{\text{w}}/T_{\text{ad}} = 1$, $x_{\text{in}} = 0.2$. □, $x_{\text{out}} = 0.25$; ■, $x_{\text{out}} = 0.3$; ○, $x_{\text{out}} = 0.35$; ●, $x_{\text{out}} = 0.4$;

at the edge of the boundary layer was calculated assuming calorically perfect gas flow at free stream Mach number $M_\infty = 6$. The calculations are performed for cone half-angles of $\theta = 15°$ and $25°$. The main goal in the presentation of the results is to discuss the effects originating from flow divergence induced by the geometry.

Figure 1 shows the objective function $G\epsilon^2$ obtained from the optimization procedure for $\theta = 15°$. Adiabatic boundary conditions are used for the temperature at the wall, $T_{\text{w}}/T_{\text{ad}} = 1$, and the initial station is kept constant, $x_{\text{in}} = 0.2$, while changing the outlet one. Results show that there exists a location, downstream of $x_{\text{in}} = 0.2$, where the curve of the maximum energy growth as a function of $\widetilde{m} = \epsilon m$ reaches the largest value, after which the maximum of the curve decreases with increasing x_{out}. Among the computed curves, the maximum gain seems to be reached for $x_{\text{out}} = 0.35$, but a better estimate can be obtained by performing a parabolic interpolation of the data available at $\beta = 0.035$. In the latter way the maximum gain is found for $x_{\text{out}} = 0.34$, i.e. for an interval $\Delta x = x_{\text{out}} - x_{\text{in}} = 0.14$. When comparing results for $x_{\text{out}} < 1$, however, it should be kept in mind that the gain is normalized with Re_{ref}, and not with Re_{out}.

Figure 2 reports the same plots as in figure 1, with the difference that the inlet location is now at $x_{\text{in}} = 0.4$. As seen before, as the outlet location x_{out} is moved downstream, the curve of optimal gain first shows an increasing maximum but after $x_{\text{out}} = 0.7$ the maximum decreases with x_{out}. In this case the estimated x_{out} that causes the maximum gain is $x_{\text{out}} = 0.67$ and the interval $\Delta x = x_{\text{out}} - x_{\text{in}} = 0.27$ is greater than the value $\Delta x = 0.14$ previously observed for an inlet location closer to the cone tip. This means that divergence effects are stronger in the proximity of $x_{\text{in}} = 0$, as one could argue from geometrical considerations.

Figure 3 shows the objective function $G\epsilon^2$ obtained for $\theta = 25°$ and inlet location $x_{\text{in}} = 0.2$. The general trend of the results is the same as in the previous case. As the outlet station is moved downstream, the maximum energy growth keeps increasing (see $x_{\text{out}} = 0.225$, $x_{\text{out}} = 0.25$ and $x_{\text{out}} = 0.275$) until a certain location at which the curve is the largest possible ($x_{\text{out}} = 0.3$), after which the maximum growth starts decreasing again ($x_{\text{out}} \geq 0.4$). For $\theta = 25°$ and $x_{\text{in}} = 0.2$ the estimated x_{out} that leads to the maximum is $x_{\text{out}} = 0.32$. The x-interval for reaching such a maximum is $\Delta x = 0.12$, which is smaller than what was seen for $\theta = 15°$ and $x_{\text{in}} = 0.2$. This implies that divergence effects are stronger for a larger angle θ.

Figure 4 shows results for $\theta = 25°$ and $x_{\text{in}} = 0.4$. The behavior of the curves is still the same as before, but the largest values of $G\epsilon^2$ are now reached for an estimated $x_{\text{out}} = 0.64$. $\Delta x = 0.24$, being smaller than $\Delta x = 0.27$ observed for $\theta = 15$, confirms the fact already seen in figure 3 that flow-divergence effects are stronger if the nose-tip angle is larger.

Figure 5 reports results for the flat plate in the same fashion as previously seen. The reason why these plots are shown is that in the flat-plate case there are no effects due to the divergence of the flow and thus

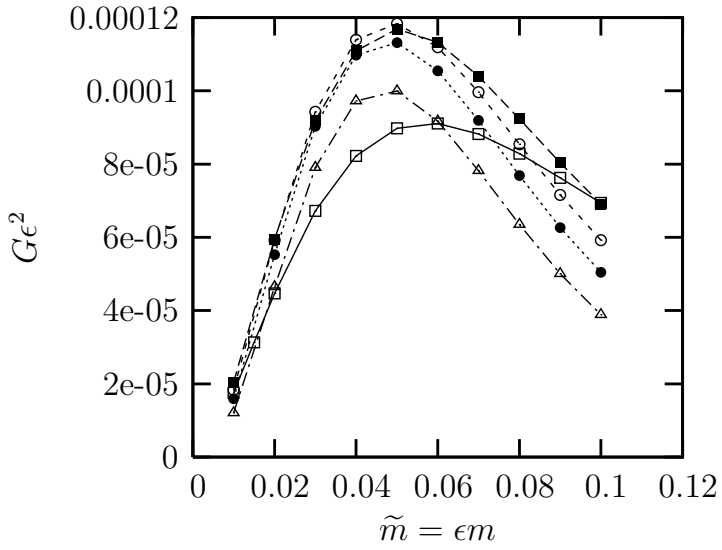

Figure 2. Objective function $G\epsilon^2$: effect of x_{out} and $\widetilde{m}$ for $\theta = 15°$, $M_\infty = 6$, $M_{\text{loc}} = 4.367$, $T_{\text{w}}/T_{\text{ad}} = 1$, $x_{\text{in}} = 0.4$. □, $x_{\text{out}} = 0.5$; ■, $x_{\text{out}} = 0.6$; ○, $x_{\text{out}} = 0.7$; ●, $x_{\text{out}} = 0.8$; Δ, $x_{\text{out}} = 1.0$.

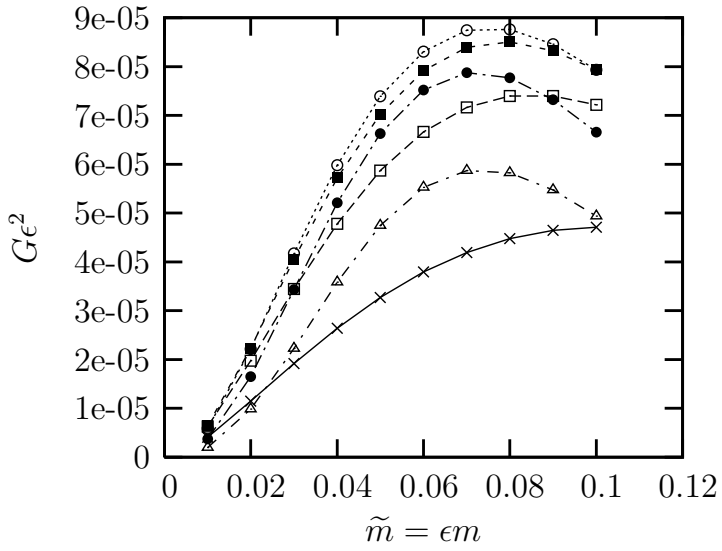

Figure 3. Objective function $G\epsilon^2$: effect of x_{out} and $\widetilde{m}$ for $\theta = 25°$, $M_\infty = 6$, $M_{\text{loc}} = 3.218$, $T_{\text{w}}/T_{\text{ad}} = 1$, $x_{\text{in}} = 0.2$. ×, $x_{\text{out}} = 0.225$; □, $x_{\text{out}} = 0.25$; ■, $x_{\text{out}} = 0.275$; ○, $x_{\text{out}} = 0.3$; ●, $x_{\text{out}} = 0.4$; Δ, $x_{\text{out}} = 0.6$.

by comparing figure 5 with the previous ones more insights can be gained regarding the influence of the geometry. Conditions in figure 5 are $M = 3.218$ (the local Mach number on the 25° cone), adiabatic wall, $x_{\text{in}} = 0.4$. It is clear that moving the outlet location downstream leads to a monotonic increase in the curve of maximum energy growth, reaching larger values as x_{out} moves downstream without a precise optimal distance from x_{in}. This is a new finding with respect to previous figures and to previously published results for flat plate,[20] in which only the inlet location x_{in} was changed, while keeping $x_{\text{out}} = 1.0$. As metioned earlier, however, when comparing results for $x_{\text{out}} < 1$ it should be remarked that the gain is normalized with Re_{ref}, and not with Re_{out}. The straightforward conclusion from the comparison between figure 5 and the previous ones is that, once the inlet location is fixed, divergence effects result in the existence of an optimal outlet location x_{out} for which the largest energy growth is reached. This behavior was present also in the

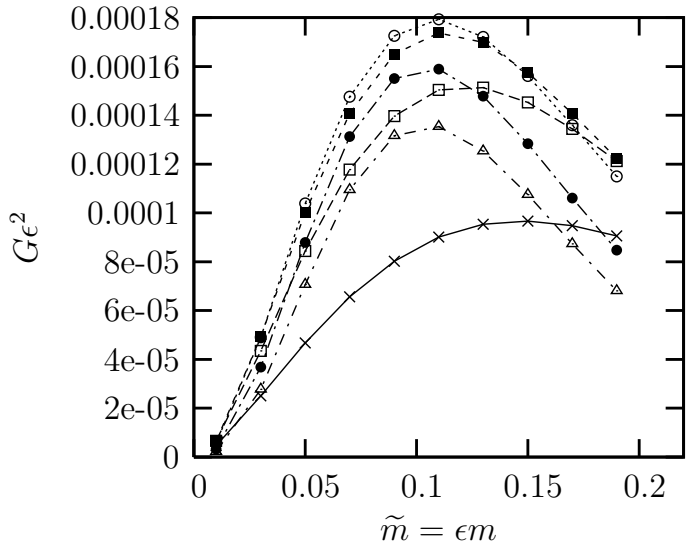

Figure 4. Objective function $G\epsilon^2$: effect of x_{out} and $\widetilde{m}$ for $\theta = 25°$, $M_\infty = 6$, $M_{\text{loc}} = 3.218$, $T_{\text{w}}/T_{\text{ad}} = 1$, $x_{\text{in}} = 0.4$. ×, $x_{\text{out}} = 0.45$; □, $x_{\text{out}} = 0.5$; ■, $x_{\text{out}} = 0.55$; ○, $x_{\text{out}} = 0.6$; ●, $x_{\text{out}} = 0.8$; Δ, $x_{\text{out}} = 1.0$.

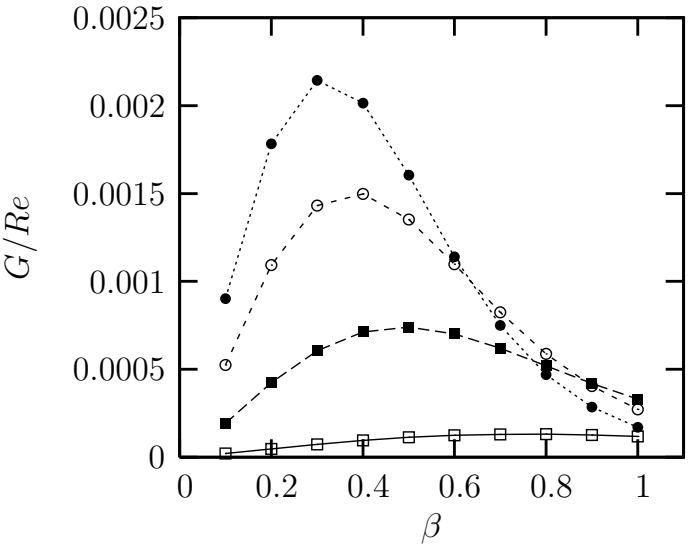

Figure 5. Objective function G/Re, flat plate: effect of x_{out} and β for $M = 3.218$, $T_{\text{w}}/T_{\text{ad}} = 1$, $x_{\text{in}} = 0.4$. □, $x_{\text{out}} = 0.45$; ■, $x_{\text{out}} = 0.55$; ○, $x_{\text{out}} = 0.6$; ●, $x_{\text{out}} = 1.0$;

sphere case,[19,10,11] corroborating the conjecture of being due to the flow divergence only.

Figure 6 plots the reverse case to what was seen before. The gain $G\epsilon^2$ is shown for the sharp-cone case, keeping the outlet location fixed, $x_{\text{out}} = 1.0$, and changing the inlet location x_{in}. The other parameters are $\theta = 25°$, $M_\infty = 6$, $M_{\text{loc}} = 3.218$, and $T_{\text{w}}/T_{\text{ad}} = 1$. Results show that the largest energy growth is obtained for $x_{\text{in}} = 0.8$, i.e. for $\Delta x = 0.2$. This is comparable with the value of Δx found before for the 25° cone, supporting once more the observation that flow-divergence effects become weaker as we move downstream.

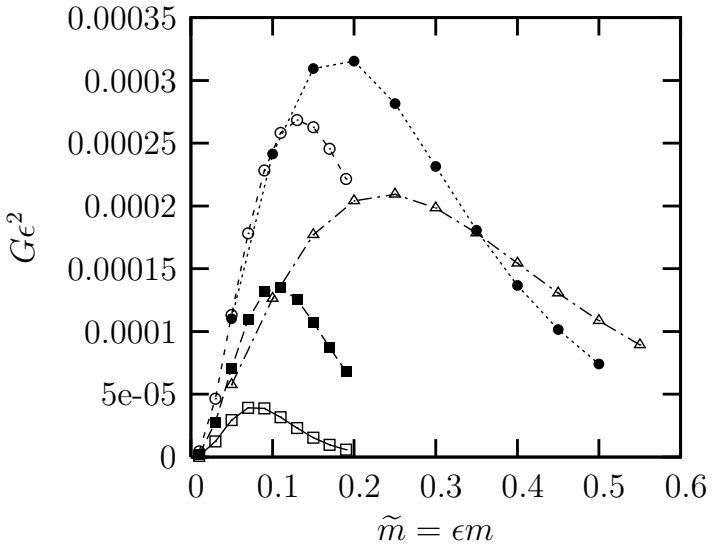

Figure 6. Objective function $G\epsilon^2$: effect of x_{in} and $\widetilde{m}$ for $\theta = 25°$, $M_\infty = 6$, $M_{\text{loc}} = 3.218$, $T_{\text{w}}/T_{\text{ad}} = 1$, $x_{\text{out}} = 1.0$. □, $x_{\text{in}} = 0.2$; ■, $x_{\text{in}} = 0.4$; ○, $x_{\text{in}} = 0.6$; ●, $x_{\text{in}} = 0.8$; Δ, $x_{\text{in}} = 0.9$.

VI. A quantitative comparison between flat-plate and sharp-cone results

Results presented in figure 5 certainly shed a new light on the differences between flat-plate and sharp-cone geometries that can be attributed to flow divergence. However, the order of magnitude of the gain reported in that figure differs quite remarkably from what shown in the figures regarding the sharp cone, allowing only a qualitative comparison. In order to compare quantitatively the energy growth for the flat plate and cone, both physics and scaling should be considered.

The physics suggests that the results for the sharp cone should reduce to those obtained for the flat plate in the limits $x_{\text{in}} \to x_{\text{out}}$ and $m \to \infty$. The first is dictated by the fact that divergence effects (which are the main difference between sharp-cone and flat-plate geometries) are negligible far from the cone tip (in the proximity of x_{out}), as proved by the plots presented in §V. Moreover, when $x_{\text{in}} \to x_{\text{out}}$ there is not enough streamwise development of the flow to let the divergence influence the results. The second limit is due to the fact the the presence of many vortices in the azimuthal direction forces the flow to be less sensitive to divergence and thus to behave like in the flat-plate case. Hence, in order to emphasize the effects of divergence in the flow past the sharp cone, we focus on the limits $x_{\text{in}} \to x_{\text{out}}$ and $m \to \infty$. The outlet location $x_{\text{out}} = 1$ is kept constant, as for the flat-plate case, so as to allow direct comparison. Changing x_{out} would imply changing the Reynolds number Re when comparing results.

The scaling is important as well. The fact that the boundary layer over the cone is $\sqrt{3}$ thinner than the boundary layer over the flat plate and the choice of the same length scale L_{ref} for the definition of the Reynolds in both cases suggest that G/Re for the flat plate[20,10,11] must be compared with $3G\epsilon^2$. On the other hand, the wavenumber $\beta z/H_{\text{ref plate}}$ must be compared with

$$m\phi = \frac{mz}{R} = \frac{mH_{\text{ref cone}}}{R}\frac{z}{H_{\text{ref cone}}},$$

where z is the transversal coordinate along the surface and R is the local radius. The comparison between $\beta z/H_{\text{ref plate}}$ and $m\phi$ therefore reduces to the comparison between β and $mH_{\text{ref cone}}/R$. However, since $H_{\text{ref cone}} = H_{\text{ref plate}}/\sqrt{3}$, and $R = L_{\text{ref}} \sin\theta$, by taking into account that $\epsilon = H_{\text{ref plate}}/L_{\text{ref}}$, one gets

$$\frac{mH_{\text{ref cone}}}{R} = \frac{mH_{\text{ref plate}}}{\sqrt{3}R} = \frac{mH_{\text{ref plate}}}{\sqrt{3}L\sin\theta} = \frac{m\epsilon}{\sqrt{3}\sin\theta} = \frac{\widetilde{m}}{\sqrt{3}\sin\theta}.$$

Figure 7 shows the gain as a function of the wavenumber for different angles θ and different intervals of $\Delta x = x_{\text{out}} - x_{\text{in}}$, for both the flat plate and sharp cone. Many conclusions can be deduced from this plot.

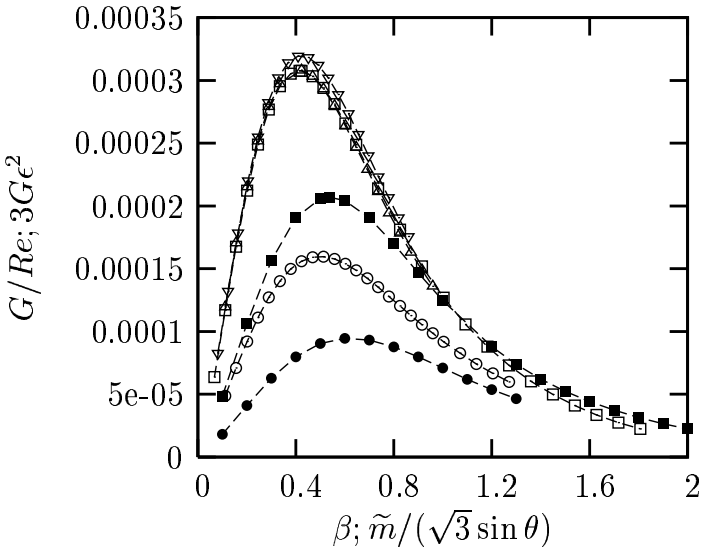

Figure 7. Objective function, comparison between G/Re (flat plate) and $3G\epsilon^2$ (sharp cone) as a function of β and $\widetilde{m}/(\sqrt{3}\sin\theta)$ respectively, effect of $x_{\rm in}$ and wavenumber. $M_{\rm loc} = 3$, $T_{\rm w}/T_{\rm ad} = 1$, $x_{\rm out} = 1.0$. □, $\theta = 15°$ **and** $x_{\rm in} = 0.95$; △, $\theta = 15°$, $x_{\rm in} = 0.95$ **and** $\epsilon = 0.0001$; ○, $\theta = 15°$ **and** $x_{\rm in} = 0.97113$; ▽, $\theta = 25°$ **and** $x_{\rm in} = 0.95$; ■, **flat plate,** $x_{\rm in} = 0.91340$; ●, **flat plate,** $x_{\rm in} = 0.95$.

First, the scaling. All results obtained for the cone in the case $x_{\rm in} = 0.95$ and $x_{\rm out} = 1.0$ (□, △, ▽, ◇) scale correctly for small values of the wavenumber, regardless of θ. This is an *a posteriori* test on the correctness of the scaling. Secondly, ϵ does not have any effect on the gain, as it is proved by the comparison between the cases $\epsilon = 0.001$ (□) and $\epsilon = 0.0001$ (△), both referring to $x_{\rm in} = 0.95$, $x_{\rm out} = 1.0$ and $\theta = 15°$. All results are obtained for $\epsilon = 0.001$, unless otherwise stated. Third, the comparison between cone (empty symbols) and flat plate (full symbols) should be carried out with further care with respect to Δx. In fact, because of the difference in the boundary layer thickness between flat plate and cone, distances Δx having about the same value in boundary-layer thicknesses should be considered. We suggest to compare $\Delta x_{\rm cone}$ with $\Delta x_{\rm plate}/\sqrt{3}$, implying that the sharp-cone cases $x \in [0.95; 1]$ and $x \in [0.97113; 1]$ should be compared respectively with the flat-plate cases $x \in [0.91340; 1]$, and $x \in [0.95; 1]$. Figure 7 confirms it by showing that results for the sharp cone and flat plate collapse onto each other for $\widetilde{m} \to \infty$, when the correct intervals Δx are considered (see □ vs. ■ and ○ vs. ●).

Figure 8 reports the comparison between sharp cone (empty symbols), $\theta = 15°$, and flat plate (full symbols) for the properly rescaled Δx (i.e. □ compares with ■, ○ with ●, △ with ▲, and ▽ with ▼). It can be noted that the difference in the energy growth between the two geometries diminishes as $x_{\rm in} \to x_{\rm out}$ (see for example the sharp-cone case $x_{\rm in} = 0.95$, ▽, compared to the flat-plate case $x_{\rm in} = 0.91340$, ▼) and $m \to \infty$, confirming what one should expect.

Figure 9 shows the effect of the wall temperature together with the comparison between the two geometries in the limits $x_{\rm in} \to x_{\rm out}$ and $m \to \infty$. Empty symbols refer to sharp cone ($\theta = 15°$) and full symbols to flat plate. It can be noted that a cold wall, i.e. $T_{\rm w}/T_{\rm ad} = 0.5$ (○ and ▽ for sharp cone, corresponding to the cases ● and ▼ for the flat plate) enhance the energy growth, as already pointed out in previous studies.[20,19,10,11] Moreover, not only the gain is larger for a cold wall, but also the wavenumber for which the optimum is reached. When comparing adiabatic versus cold wall results, it should be noted that in the cold case the gain is larger for small values of the wavenumber, while is becomes smaller for larger wavenumbers (see for instance the cases ○ and ●, for which the discriminating wavenumber is about $\beta \approx 1.05$). Moreover, for very large values of the wavenumber, results for the two geometries collapse onto each other, as a consequence of the $m \to \infty$ limit previously described. This behavior is consistent, for each case considered (see also □ vs. ■, and ▽ vs. ▼).

Figure 10 reproduces the behavior of the energy growth (including only the perturbations u and T) as a function of the streamwise coordinate, where the latter is properly rescaled so as to allow a direct comparison between the sharp-cone case $\theta = 15°$, $x \in [0.95; 1.0]$ (solid line) and the flat-plate case $x \in [0.91340; 1.0]$

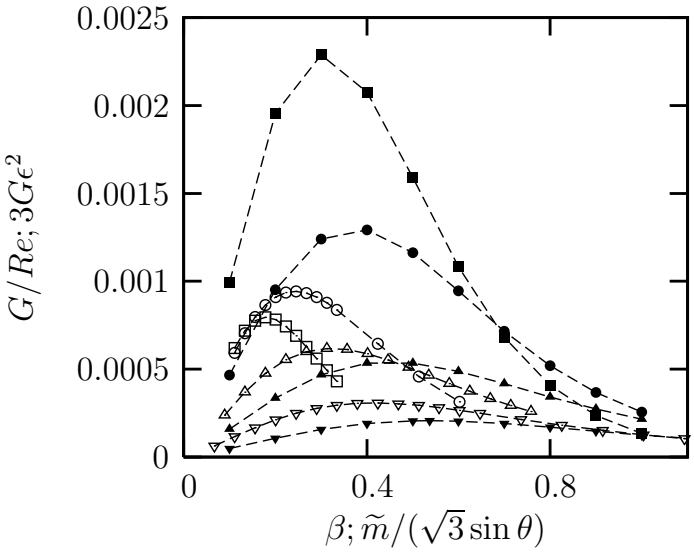

Figure 8. Objective function, comparison between G/Re (flat plate, full symbols) and $3G\epsilon^2$ (sharp cone, empty symbols) as a function of β and $\widetilde{m}/(\sqrt{3}\sin\theta)$ respectively, effect of $x_{\rm in}$ and wavenumber. $M_{\rm loc} = 3$, $T_{\rm w}/T_{\rm ad} = 1$, $x_{\rm out} = 1.0$. **Sharp cone:** □, $\theta = 15°$ **and** $x_{\rm in} = 0.6$; ○, $\theta = 15°$ **and** $x_{\rm in} = 0.8$; △, $\theta = 15°$ **and** $x_{\rm in} = 0.9$; ▽, $\theta = 15°$ **and** $x_{\rm in} = 0.95$. **Flat plate:** ■, $x_{\rm in} = 0.30718$; ●, $x_{\rm in} = 0.65359$; ▲, $x_{\rm in} = 0.82679$; ▼, $x_{\rm in} = 0.91340$.

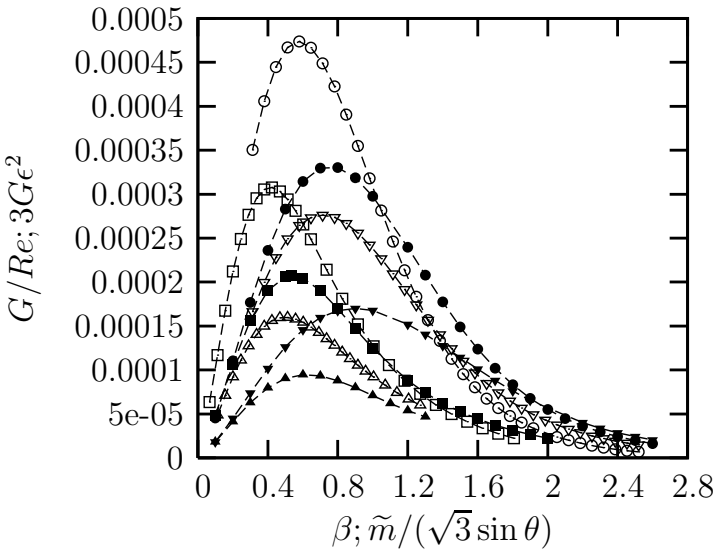

Figure 9. Objective function, comparison between G/Re (flat plate, full symbols) and $3G\epsilon^2$ (sharp cone, empty symbols) as a function of β and $\widetilde{m}/(\sqrt{3}\sin\theta)$ respectively, effect of $x_{\rm in}$, wavenumber and $T_{\rm w}/T_{\rm ad}$. $M_{\rm loc} = 3$, $x_{\rm out} = 1.0$. **Sharp cone:** □, $\theta = 15°$, $T_{\rm w}/T_{\rm ad} = 1.0$ **and** $x_{\rm in} = 0.95$; ○, $\theta = 15°$, $T_{\rm w}/T_{\rm ad} = 0.5$ **and** $x_{\rm in} = 0.95$; △, $\theta = 15°$, $T_{\rm w}/T_{\rm ad} = 1.0$ **and** $x_{\rm in} = 0.97113$; ▽, $\theta = 15°$, $T_{\rm w}/T_{\rm ad} = 0.5$ **and** $x_{\rm in} = 0.97113$. **Flat plate:** ■, $x_{\rm in} = 0.91340$ **and** $T_{\rm w}/T_{\rm ad} = 1.0$; ●, $x_{\rm in} = 0.91340$ **and** $T_{\rm w}/T_{\rm ad} = 0.5$; ▲, $x_{\rm in} = 0.95$ **and** $T_{\rm w}/T_{\rm ad} = 1.0$; ▼, $x_{\rm in} = 0.95$ **and** $T_{\rm w}/T_{\rm ad} = 0.5$.

(dashed line). Since the comparison is done at the optimal wavenumbers ($\widetilde{m} = 0.186$ and $\beta = 0.537$), the energy grows monotonically with the streamwise coordinate[23, 14]

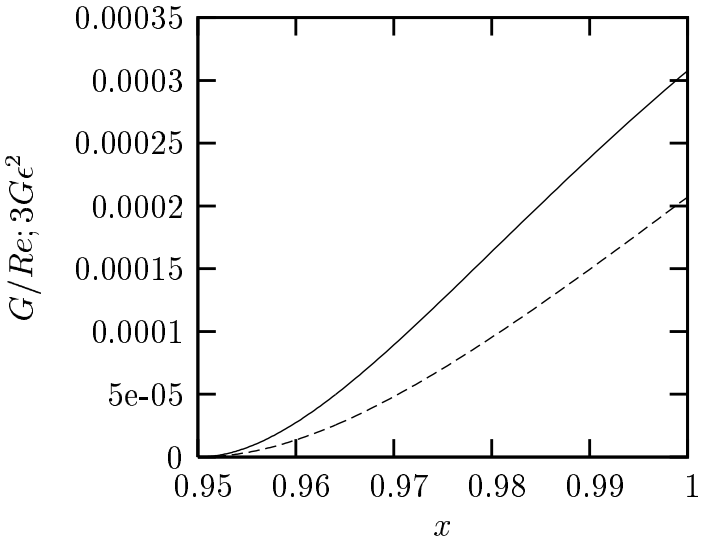

Figure 10. Energy (u^2, T^2) as a function of the streamwise coordinate $x_{\rm cone}$. Comparison between G/Re (flat plate, dash line) and $3G\epsilon^2$ (sharp cone, solid line) at the optimal wavenumbers $\widetilde{m} = 0.186$ and $\beta = 0.537$ for $\theta = 15°$, $M_{\rm loc} = 3$, $x_{\rm out} = 1.0$, $T_{\rm w}/T_{\rm ad} = 1$. For the flat plate, x has been rescaled as $x_{\rm plate_{out}} - (x_{\rm plate_{out}} - x)/\sqrt{3}$.

VII. Conclusion

Optimal disturbances originating in the supersonic boundary-layer flow past a sharp axisymmetric cone have been studied.

Such a geometry is motivated by several factors. Similar studies previously published[20,19,10,11] reported optimal perturbations for flat plate and sphere, with the consequence that a direct comparison between them is extremely complicated due to the many effects present in the case of the sphere (flow divergence, centrifugal forces and dependence of the edge parameters on the local Mach number). The sharp cone, on the other hand, represents a simpler geometry characterized by flow-divergence effects only (with respect to the case of flat plate), allowing us to identify these effects. Moreover, in the development of the studies towards a more realistic three-dimensional supersonic case, the sharp cone geometry represents a natural step before the blunt-nose cone geometry.

Equations are obtained from the linearized Navier–Stokes equations by employing a scaling that assumes the perturbation dominated by streamwise vortices. This leads to parabolic-in-x equations. The optimization is carried out in an iterative manner, relying on the alternate solution of the direct and adjoint problems related by coupling conditions at the inlet and outlet.

Results are carried out for different conditions.

A first set is obtained by keeping the inlet location fixed and changing the outlet location. An optimal distance from the inlet is found, for which the curve of the maximum gain is the largest. This Δx ($\Delta x = x_{\rm out} - x_{\rm in}$) increases when the inlet location is moved downstream, proving that divergence effects are stronger in the proximity of the cone tip. Increasing the half-cone angle leads to a decrease of Δx (compared for the same values of $x_{\rm in}$), supporting the intuitive idea that for larger angles divergence effects are stronger. When these results are compared with the case of the flat plate, it becomes clear that the presence of an optimal downstream location for the energy growth is an unique characteristic of flows dominated by geometrical divergence, such as sharp cone and sphere. For the flat plate case, in fact, given an inlet station $x_{\rm in}$, the curve of optimal energy gain reaches larger values monotonically as the outlet location is moved downstream, contrary to the cases of sharp cone and sphere.

A second set of results in obtained keeping the outlet location fixed and changing the inlet one. The gain, wavenumber and Δx are properly rescaled taking into account the half-cone angle θ and the fact that the boundary layer on the sharp cone is $\sqrt{3}$ thinner than the one over the flat plate. By comparing the two geometries, it is found that both the gain and the wavenumber scale fairly well and that results for the sharp cone collapse into those for the flat plate in the limits $x_{\rm in} \to x_{\rm out}$ and $m \to \infty$.

Results show also that a cold wall enhances transient growth.

References

[1]Reshotko, E., "Transient growth: a factor in bypass transition," *Phys. Fluids*, Vol. 13, 2001, pp. 1067–1075.

[2]Ellingsen, T. and Palm, E., "Stability of linear flow," *Phys. Fluids*, Vol. 18, 1975, pp. 487–488.

[3]Hultgren, L. S. and Gustavsson, L. H., "Algebraic growth of disturbances in a laminar boundary layer," *Phys. Fluids*, Vol. 24, No. 6, 1981, pp. 1000–1004.

[4]Farrell, B., "Optimal excitation of perturbations in viscous shear flow," *Phys. Fluids*, Vol. 31, No. 8, 1988, pp. 2093–2102.

[5]Boberg, L. and Brosa, U., "Onset of turbulence in a pipe," *Z. Natursforschung*, Vol. 43a, 1988, pp. 697–726.

[6]Butler, K. M. and Farrell, B., "Three–dimensional optimal perturbations in viscous shear flow," *Phys. Fluids A*, Vol. 4, 1992, pp. 1637–1650.

[7]Gustavsson, L. H., "Energy growth of three-dimensional disturbances in plane Poisuille flow," *J. Fluid Mech.*, Vol. 224, 1991, pp. 241–260.

[8]Reddy, S. C. and Henningson, D. S., "Energy growth in viscous channel flows," *J. Fluid Mech.*, Vol. 252, 1993, pp. 209–238.

[9]Trefethen, L. N., Trefethen, A. E., Reddy, S. C., and Driscoll, T. A., "Hydrodynamic Stability without Eigenvalues," *Science*, Vol. 261, 1993, pp. 578–584.

[10]Zuccher, S., Tumin, A., and Reshotko, E., "Parabolic Approach to Optimal Perturbations in Compressible Boundary Layers," *J. Fluid Mech.*, 2005, (Accepted).

[11]Zuccher, S., Tumin, A., and Reshotko, E., "Optimal Disturbances in Compressible Boundary Layers – Complete Energy Norm Analysis," AIAA Paper AIAA-2005-5314, 2005.

[12]Andersson, P., Berggren, M., and Henningson, D. S., "Optimal disturbances and bypass transition in boundary layers," *Phys. Fluids*, Vol. 11, 1999, pp. 134–150.

[13]Luchini, P., "Reynolds–number–independent instability of the boundary layer over a flat surface: optimal perturbations," *J. Fluid Mech.*, Vol. 404, 2000, pp. 289–309.

[14]Zuccher, S., Bottaro, A., and Luchini, P., "Algebraic growth in a Blasius boundary layer: Nonlinear optimal disturbances." *Eur. J. Mech. B/Fluids*, Vol. 25, 2006, pp. 1–17.

[15]Hanifi, A., Schmidt, P. J., and Henningson, D., "Transient growth in compressible boundary layer flow," *Phys. Fluids*, Vol. 8, No. 3, 1996, pp. 51–65.

[16]Hanifi, A. and Henningson, D., "The compressible inviscid algebraic instability for streamwise independent disturbances," *Phys. Fluids*, Vol. 10, No. 8, 1998, pp. 1784–1786.

[17]Reshotko, E. and Tumin, A., "The blunt body paradox – A case for transient growth," *Laminar–Turbulent Transition*, Springer–Verlag, Berlin, 2000, pp. 403–408, Paper presented at the 5th IUTAM Symposium on Laminar-Turbulent Transition, Sedona, USA, 1999.

[18]Tumin, A. and Reshotko, E., "Spatial Theory of optimal disturbances in boundary layers," *Phys. Fluids*, Vol. 13, No. 7, 2001, pp. 2097–2104.

[19]Tumin, A. and Reshotko, E., "Optimal disturbances in the boundary layer over a sphere," AIAA Paper AIAA–2004–2241, 2004.

[20]Tumin, A. and Reshotko, E., "Optimal disturbances in compressible boundary layers," *AIAA J.*, Vol. 41, No. 12, 2003, pp. 2357–2363.

[21]Reshotko, E. and Tumin, A., "The role of transient growth in roughness-induced transition," *AIAA J.*, Vol. 42, No. 4, 2004, pp. 766–770.

[22]Cathalifaud, P. and Luchini, P., "Algebraic growth in boundary layers: optimal control by blowing and suction at the wall," *Eur. J. Mech. B – Fluids*, Vol. 19, 2000, pp. 469–490.

[23]Zuccher, S., Luchini, P., and Bottaro, A., "Algebraic growth in a Blasius boundary layer: optimal and robust control by mean suction in the nonlinear regime," *J. Fluid Mech.*, Vol. 513, 2004, pp. 135–160.

[24]Mack, L. M., "Boundary Layer Stability Theory," JPL Report 900-277, Jet Propulsion Lab., California Institute of Technology, Pasadena, CA, USA, 1969.

[25]Ting, L., "On the initial conditions for boundary layer equations," *J. Math. Phys.*, Vol. 44, 1965, pp. 353–367.

[26]Luchini, P. and Bottaro, A., "Görtler vortices: a backward–in–time approach to the receptivity problem," *J. Fluid Mech.*, Vol. 363, 1998, pp. 1–23.

[27]Zuccher, S., Bottaro, A., and Luchini, P., "Algebraic growth in a Blasius boundary layer: Nonlinear optimal disturbances." *Eur. J. Mech. B/Fluids*, Vol. 25, 2006, pp. 1–17.

[28]Landahl, M. T., "A note on an algebraic instability of inviscid parallel shear flow," *J. Fluid Mech.*, Vol. 98, 1980, pp. 243–251.

[29]Luchini, P. and Bottaro, A., "Linear stability and receptivity analyses of the Stokes layer produced by an impulsively started plate," *Phys. Fluids*, Vol. 13, 2001, pp. 1668–1678.

[30]Hayes, W. D. and Probstein, R. F., *Hypersonic Flow Theory*, Academic Press, New York, 1959.

A. Matrices for compressible flow past a sharp cone

Assuming that the basic flow is known, let x, y and ϕ denote the three independent coordinates, where x is the streamwise distance from the nose tip, y the wall-normal distance and ϕ the azimuthal angle. With

this notation, u, v, w are the corresponding velocity field, that together with temperature T and pressure p form the set of problem's unknowns. Density ρ is related to T and p by the state equation and thus is not an explicit unknown.

The scaling is as described in §II. The unknowns in the disturbance equations are only five and are assumed to be proportional to $\exp(im\phi)$, where m is the azimuthal index and i the imaginary unit.

In what follows viscosity μ_s is assumed to be a function of temperature only, and therefore μ_s' stands for the derivative $d\mu_s/dT_s$.

Transformations of the linearized equations lead to the system of partial differential equations

$$(\boldsymbol{A}\mathbf{f})_x = (\boldsymbol{D}\mathbf{f}_y)_x + \boldsymbol{B}_0\mathbf{f} + \boldsymbol{B}_1\mathbf{f}_y + \boldsymbol{B}_2\mathbf{f}_{yy}, \tag{1}$$

where $\boldsymbol{A}$, $\boldsymbol{B}_0$, $\boldsymbol{B}_1$, $\boldsymbol{B}_2$ and $\boldsymbol{D}$ are 5×5 matrices, and can be recast as

$$(\boldsymbol{H}_1\mathbf{f})_x + \boldsymbol{H}_2\mathbf{f} = 0. \tag{2}$$

Operators $\boldsymbol{H}_1$ and $\boldsymbol{H}_2$ are still 5×5 matrices and contain the dependence on x and y:

$$\boldsymbol{H}_1 = \boldsymbol{A} - \boldsymbol{D}(\cdot)_y; \qquad \boldsymbol{H}_2 = -\boldsymbol{B}_0 - \boldsymbol{B}_1(\cdot)_y - \boldsymbol{B}_2(\cdot)_{yy}. \tag{3}$$

The expression to be maximized, in the limit $\epsilon \to 0$ (i.e. $Re \to \infty$), is the integral in the wall-normal direction of the kinetic energy and temperature. After the transformations imposed by the geometry, E_{out} reads

$$E_{\text{out}} = \int_0^\infty \sin\theta(x + \epsilon y\cot\theta)\left[\rho_{s\,\text{out}}u_{\text{out}}^2 + + \frac{p_{s\,\text{out}}T_{\text{out}}^2}{(\gamma-1)T_{s\,\text{out}}^2 M^2}\right] dy, \tag{4}$$

where the term $\sin\theta(x + \epsilon y\cot\theta)$ stems from the integration over the whole domain, i.e. over the three independent variables.

The nonzero elements of the matrices are here reported, with the wavenumber β defined as $\beta = \widetilde{m}/(x + \epsilon y\cot\theta)$, $\widetilde{m}$ being $\widetilde{m} = \epsilon m$.

Continuity equation:

$$A^{11} = \rho_s;$$
$$A^{14} = -\frac{\rho_s U_s}{T_s};$$
$$B_0^{11} = -\frac{\rho_s}{(x + \epsilon y\cot\theta)};$$
$$B_0^{12} = -\frac{\partial\rho_s}{\partial y};$$
$$B_0^{13} = -\beta\rho_s;$$
$$B_0^{14} = \frac{\partial}{\partial y}\left(\frac{\rho_s V_s}{T_s}\right) + \frac{\rho_s U_s}{T_s(x + \epsilon y\cot\theta)}$$
$$B_1^{13} = -\rho_s;$$
$$B_1^{14} = \frac{\rho_s V_s}{T_s};$$

x-momentum equation:

$$A^{21} = 2\rho_s U_s;$$
$$A^{24} = -\frac{\rho_s U_s^2}{T_s};$$
$$B_0^{21} = -\frac{\partial\rho_s V_s}{\partial y} - \mu_s\beta^2 - \frac{2\rho_s U_s}{(x + \epsilon y\cot\theta)}$$
$$B_0^{22} = -\frac{\partial\rho_s U_s}{\partial y}$$
$$B_0^{23} = -\beta\rho_s U_s;$$
$$B_0^{24} = \frac{\partial}{\partial y}\left(\frac{\rho_s V_s U_s}{T_s}\right) + \frac{\partial}{\partial y}\left(\mu_s'\frac{\partial U_s}{\partial y}\right) + \frac{\rho_s U_s^2}{T_s(x + \epsilon y\cot\theta)}$$
$$B_1^{21} = \frac{\partial\mu_s}{\partial y} - \rho_s V_s;$$
$$B_1^{22} = -\rho_s U_s;$$

$$B_1^{24} = \frac{\rho_s U_s V_s}{T_s} + \mu_s' \frac{\partial U_s}{\partial y};$$
$$B_2^{21} = \mu_s;$$

y-momentum equation:

$$A^{31} = \rho_s V_s + \frac{2}{3}\frac{\partial \mu_s}{\partial y};$$
$$A^{32} = \rho_s U_s;$$
$$A^{34} = -\frac{\rho_s U_s V_s}{T_s} - \mu_s' \frac{\partial U_s}{\partial y};$$
$$B_0^{31} = \frac{2}{3}\frac{\partial}{\partial x}\left(\frac{\partial \mu_s}{\partial y}\right) + \frac{1}{(x + \epsilon y \cot\theta)}\left(-\frac{2}{3}\frac{\partial \mu_s}{\partial y} - \rho_s V_s\right)$$
$$B_0^{32} = -2\frac{\partial \rho_s V_s}{\partial y} - \beta^2 \mu_s - \frac{\rho_s U_s}{(x + \epsilon y \cot\theta)}$$
$$B_0^{33} = -\beta \rho_s V_s - \frac{2\beta}{3}\frac{\partial \mu_s}{\partial y};$$
$$B_0^{34} = \frac{1}{(x + \epsilon y \cot\theta)}\left[\frac{\rho_s U_s V_s}{T_s} + \frac{1}{3}\mu_s' \frac{\partial U_s}{\partial y} - \frac{2}{3}U_s \frac{\partial \mu_s'}{\partial y}\right] + \frac{\partial}{\partial y}\left(\frac{\rho_s V_s^2}{T_s}\right)$$
$$+ \frac{\partial \mu_s'}{\partial y}\left[\frac{4}{3}\frac{\partial V_s}{\partial y} - \frac{2}{3}\frac{\partial U_s}{\partial x}\right] + \mu_s'\left[-\frac{\partial}{\partial x}\left(\frac{\partial U_s}{\partial y}\right) + \frac{4}{3}\frac{\partial^2 V_s}{\partial y^2} + \frac{1}{3}\frac{\partial^2 U_s}{\partial x \partial y}\right]$$
$$B_1^{31} = \frac{\mu_s}{3(x + \epsilon y \cot\theta)} + \frac{2}{3}\frac{\partial \mu_s}{\partial x};$$
$$B_1^{32} = -2\rho_s V_s + \frac{4}{3}\frac{\partial \mu_s}{\partial y};$$
$$B_1^{33} = \frac{\beta \mu_s}{3};$$
$$B_1^{34} = \mu_s'\left[\frac{4}{3}\frac{\partial V_s}{\partial y} - \frac{2}{3}\frac{\partial U_s}{\partial x}\right] + \frac{\rho_s V_s^2}{T_s} - \frac{2U_s}{3(x + \epsilon y \cot\theta)}\mu_s'$$
$$B_1^{35} = -1;$$
$$B_2^{32} = \frac{4}{3}\mu_s;$$
$$D^{31} = \frac{\mu_s}{3};$$

ϕ-momentum equation:

$$A^{43} = \rho_s U_s;$$
$$A^{44} = \frac{\mu_s \beta U_s}{3T_s};$$
$$B_0^{41} = \frac{\mu_s \beta}{3\rho_s}\frac{\partial \rho_s}{\partial x} - \beta \frac{\partial \mu_s}{\partial x} - \frac{2\beta \mu_s}{(x + \epsilon y \cot\theta)}$$
$$B_0^{42} = \frac{\mu_s \beta}{3\rho_s}\frac{\partial \rho_s}{\partial y} - \beta \frac{\partial \mu_s}{\partial y}$$
$$B_0^{43} = -\beta^2 \mu_s - \frac{\partial \rho_s V_s}{\partial y} - \frac{2\rho_s U_s}{(x + \epsilon y \cot\theta)};$$
$$B_0^{44} = -\frac{\beta \mu_s}{3\rho_s}\frac{\partial}{\partial y}\left(\frac{\rho_s V_s}{T_s}\right) + \frac{\rho_s U_s \beta}{3T_s}\frac{\partial}{\partial x}\left(\frac{\mu_s}{\rho_s}\right) - \frac{\mu_s U_s \beta}{3T_s(x + \epsilon y \cot\theta)}$$
$$+ \frac{2\beta \mu_s'}{3}\frac{\partial U_s}{\partial x} + \frac{2\beta \mu_s'}{3}\frac{\partial V_s}{\partial x} - \frac{4\beta U_s \mu_s'}{3(x + \epsilon y \cot\theta)};$$
$$B_0^{45} = \beta;$$
$$B_1^{43} = -\rho_s V_s + \frac{\partial \mu_s}{\partial y};$$
$$B_1^{44} = -\frac{\beta \mu_s V_s}{3T_s};$$
$$B_2^{43} = \mu_s;$$

Energy equation:

$$A^{51} = \rho_s T_s;$$

$$
\begin{aligned}
B_0^{51} &= \frac{\gamma-1}{\gamma}\frac{\partial p_s}{\partial x} - \frac{\rho_s T_s}{(x+\epsilon y\cot\theta)};\\
B_0^{52} &= -\frac{\partial \rho_s T_s}{\partial y};\\
B_0^{53} &= -\beta \rho_s T_s;\\
B_0^{54} &= \mu_s'(\gamma-1)M_{\text{ref}}^2\left(\frac{\partial U_s}{\partial y}\right)^2 - \frac{\beta^2\mu_s}{Pr} + \frac{1}{Pr}\frac{\partial}{\partial y}\left(\mu_s'\frac{\partial T_s}{\partial y}\right);\\
B_1^{51} &= 2(\gamma-1)M_{\text{ref}}^2\mu_s\frac{\partial U_s}{\partial y};\\
B_1^{52} &= -\rho_s T_s;\\
B_1^{54} &= \frac{2}{Pr}\frac{\partial \mu_s}{\partial y};\\
B_2^{54} &= \frac{\mu_s}{Pr}.
\end{aligned}
$$